Bending of elastic fibres in viscous flows: the influence of confinement[‡]

Jason S. Wexler[1,3,†], **Philippe H. Trinh**[2], **Helene Berthet**[3], **Nawal Quennouz**[3], **Olivia du Roure**[3], **Herbert E. Huppert**[4,5], **Anke Lindner**[3] **and Howard A. Stone**[1]

[1]Department of Mechanical and Aerospace Engineering, Princeton University, Princeton, NJ 08544, USA

[2]Program in Applied and Computational Mathematics, Princeton University, Princeton, NJ 08544, USA

[3]PMMH, ESPCI, CNRS UMR 7636, Université Pierre et Marie Curie, Université Paris Diderot, 10 rue Vauquelin, 75005 Paris, France

[4]Institute of Theoretical Geophysics, Department of Applied Mathematics and Theoretical Physics, University of Cambridge, Wilberforce Road, Cambridge CB3 0WA, UK

[5]School of Mathematics, University of New South Wales, Kensington, NSW 2052, Australia

We present a mathematical model and corresponding series of microfluidic experiments examining the flow of a viscous fluid past an elastic fibre in a three-dimensional channel. The fibre's axis lies perpendicular to the direction of flow and its base is clamped to one wall of the channel; the sidewalls of the channel are close to the fibre, confining the flow. Experiments show that there is a linear relationship between deflection and flow rate for highly confined fibres at low flow rates, which inspires an asymptotic treatment of the problem in this regime. The three-dimensional problem is reduced to a two-dimensional model, consisting of Hele-Shaw flow past a barrier, with boundary conditions at the barrier that allow for the effects of flexibility and three-dimensional leakage. The analysis yields insight into the competing effects of flexion and leakage, and an analytical solution is derived for the leading-order pressure field corresponding to a slit that partially blocks a two-dimensional channel. The predictions of our model show favourable agreement with experimental results, allowing measurement of the fibre's elasticity and the flow rate in the channel.

1. Introduction

An anchored elastic fibre will bend when held perpendicular to the flow of a viscous fluid. The degree of bending varies with material properties of the fibre and the fluid, the flow rate and the surrounding geometry. In particular, we consider a fibre that is anchored in a rectangular channel, with the walls of the channel positioned near the fibre and thereby confining the flow. We present experiments for this system and demonstrate how the three-dimensional geometry can be reduced to a two-dimensional model, and how quantities such as fibre deflection and velocity fields can be derived with the use of asymptotic and numerical methods.

† Email addresses for correspondence: jwexler@princeton.edu, anke.lindner@espci.fr, hastone@princeton.edu

The study of fluid–structure interactions has a rich history, although the majority of research has focused on flows at high Reynolds numbers (cf. Païdoussis 2004). An example giving recent insight into such problems is the work of Alben, Shelley & Zhang (2002), which shows how the drag induced by an anchored deformable fibre differs from the traditional drag induced by rigid objects. In contrast, a number of papers study the dynamics of an elastic fibre submerged in a flow at low Reynolds number (Stokes flow). The fibre can be, for example, freely flowing (Stockie & Green 1998; Joung, Phan-Thien & Fan 2001; Wandersman *et al.* 2010), experiencing a body force (Cosentino Lagomarsino, Pagonabarraga & Lowe 2005), forced with a prescribed end motion (Wiggins & Goldstein 1998; Yu, Lauga & Hosoi 2006; Qian, Powers & Breuer 2008) or held with one end anchored (Autrusson *et al.* 2011; Pozrikidis 2011; Guglielmini *et al.* 2012; Young, Downs & Jacobs 2012).

A complication not emphasized in the above low-Reynolds-number studies is the effect of a confining geometry on the resultant flow fields, and the corresponding influence on fibre deformation (e.g. Berthet 2012). In examples ranging from bacteria motion (DiLuzio *et al.* 2005) to micro-pumps (Day & Stone 2000), confinement has been shown to have a significant effect. Indeed, the recent work of Semin, Hulin & Auradou (2009) focusses on how the drag on a fixed rigid cylinder varies depending on the degree of geometrical confinement. Our goal then is to study the influence of confinement on the dynamics of an elastic fibre in low-Reynolds-number flow.

Our study has practical implications, with many possible applications in the field of microfluidics (cf. the reviews by Stone, Stroock & Ajdari 2004 and Squires & Quake 2005). Attia *et al.* (2009), for example, show how thin deformable structures with a spring-like geometry, anchored in the centre of a microfluidic channel, can be used as sensors to measure flow rate. In their study the deformation of the sensor is calibrated experimentally against known flow rates, to obtain a relationship between deformation and flow rate. Thin flexible structures are also prevalent in biology, with examples including cilia and flagella, which are primary appendages for feeding and propulsion for many types of cells (Lauga & Powers 2009). Our analysis could bring insight to the dynamics of cell motility and feeding in confined flow. As an additional example, Rusconi *et al.* (2010) report the growth of flexible fibre-like biofilm structures, which originate from wall-anchored biofilms located near the corners of micro-channels.

We begin this paper by describing, in §2, our microfluidic experiments that motivate the study. The geometry, shown schematically in figure 1, is chosen to highlight the effects of confinement on fibre bending, as well as potentially to offer a method of flow measurement along the lines of Attia *et al.* (2009). In §3, we propose a mathematical model for the corresponding low-Reynolds-number flow, which focuses on the particular case of weakly deflected fibres, when only a small amount of fluid passes between the fibre and the laterally confining channel walls. This step allows a reduction of the three-dimensional geometry to a two-dimensional model, which is further studied using asymptotic analysis in §4, as well as numerical methods in §5. We offer a comparison to experimental results in §6 and conclude in §7 with a summary of the implications of our analysis.

2. Experiment

The experimental geometry consists of a long rectangular channel of large aspect ratio, with a rectangular fibre extending from one of the sidewalls as shown schematically in figure 1. The fluid flows in the *x*-direction, the fibre extends in the *y*-direction and the channel is thin in the *z*-direction. The fibre is flexible, both
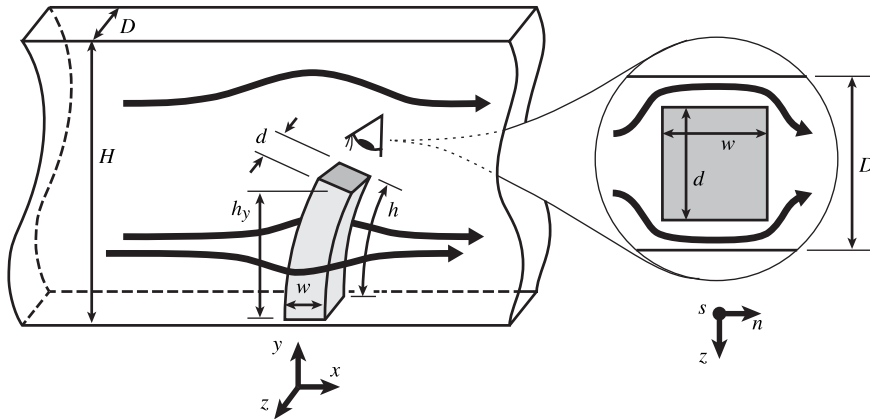
FIGURE 1. Schematic of a planform view of the channel geometry (left), and a cross-sectional view down the axis of the fibre (right). In experiments the very tip of the fibre is rounded; it is shown square in this schematic for clarity in defining the dimensions.

because of its slenderness and because it is made of a soft material. We pump a Newtonian fluid through the channel at known flow rates and record the shape that the fibre takes as in the inset of figure 2. Experiments are performed over a broad range of flow rates, but in this work we focus on small deflections of the fibre.

2.1. *Experimental methods*

The rectangular microfluidic channel is made of polydimethylsiloxane (PDMS, General Electric) and has a depth $D = 66$ µm and a height $H = 400$ µm (see figure 1). The channels are approximately 3 cm long and are moulded on a silicone wafer using standard soft-lithography techniques. The fabrication allows for features such as walls and pillars that span the entire depth of the channel, but features such as the fibre, which only partially block the depth, present a difficulty and necessitate a different fabrication method.

We implement the technique of 'stop-flow lithography', as introduced by Dendukuri *et al.* (2007), and succeed in making highly confined fibres that are anchored in the channel. We follow the fibre polymerization methods of Berthet (2012), first filling the channel with a photo-curable solution of 90 wt% polyethylene glycol diacrylate, with average molecular weight 575 (PEGDA-575, Aldrich Chemistry) and 10 wt% 2-hydroxy-2-methylpropiophenone photo-initiator (Aldrich Chemistry). Great care is taken in preparing the solution so as to eliminate irreproducibilities in the polymerization process. A fresh solution is mixed before each experiment, nitrogen is run through the solution for 30 min to purge dissolved oxygen, and then the solution is degassed for 30 min to remove nitrogen bubbles. A photomask with the desired fibre geometry is placed in the light path of the fluorescence lamp (X-Cite) on a microscope (Zeiss) at 10× magnification, and the shutter is opened for 225 ms. This procedure cures the unmasked portion of the solution in the channel. The exposure time was determined to give the most accurate reproduction of the desired fibre geometry with our specific set-up.

When the shutter is open, the entire depth of the channel not blocked by the mask is exposed to ultraviolet light. The polymerization reaction can only occur away from PDMS surfaces however, since the reaction is inhibited by dissolved oxygen
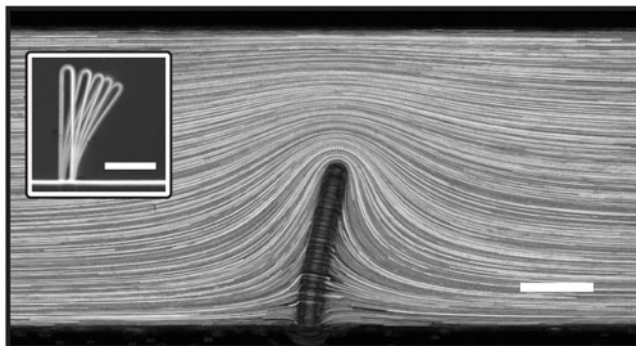
FIGURE 2. Particle paths from a channel with fibre height $h = 226$ µm, fibre width $w = 31$ µm and fibre depth $d = 34$ µm. The channel has height $H = 400$ µm, depth $D = 45$ µm and flow rate $Q = 3$ µL min^{-1}. The inset displays phase contrast images of the same fibre without tracer particles, for flow rates of $Q = 0$, 3, 8, 15 and 30 µL min^{-1} (left to right). The higher flow rates are included here for illustrative purposes, and are not considered to be in the linear regime of our model. Scale bars are 100 µm.

and PDMS is permeable to oxygen. Therefore, next to all surfaces there exists a thin 'inhibition layer' that cannot be polymerized (Dendukuri *et al.* 2008). The existence of the inhibition layer allows us to create a fibre that partially blocks the channel depth, but it also presents a difficulty in mounting the fibre because there is a similar inhibition layer next to lateral walls. To overcome this issue, we polymerize the fibre so that it attaches to a wall that is also polymerized from PEGDA. The wall, in turn, is anchored with multiple PDMS posts and gives the fibre a clamped boundary condition at its base (see Attia *et al.* (2009) for a similar example using one post).

We observe the inhibition layer to be approximately 5–6 µm, based on observations that $D - d \approx 10$–12 µm (accounting for an inhibition layer on both the top and bottom surfaces), where D is the depth of the channel and d is the depth of the fibre (see figure 1). The channel depth is measured on the silicon mould using a mechanical profilometer (Dektak). The fibre depth is measured optically, by polymerizing unanchored fibres in the channel, and applying flow so that they flip to their side. The cross-section of the fibre is observed to be rectangular, but the very tip is slightly rounded in the *xy*-plane as shown in the microscope images of figure 2. In our experiments, the fibre width, w, varies from 22 to 34 µm, and the fibre height, h, varies from 144 to 293 µm. A value for the Young's modulus of a material polymerized under these specific cross-linking conditions could not be found in the literature (measurements under different cross-linking conditions can be found in the work of Berthet (2012)). Thus, we use our model to extract the Young's modulus as discussed in § 6.

In our experiments, we pump a solution of 100 wt% PEGDA-575 through the channels and measure the deflection of the tip of the fibre at varying flow rates. We use this solution to guarantee that the polymerized fibre, which is a gel, does not swell, and to avoid accidental polymerization that might occur if the photo-initiator were included in the solution. The density of the solution is reported by the manufacturer to be $\rho = 1.12$ g mL^{-1}. The kinematic viscosity of the solution was measured with a capillary viscometer (Schott) to be $\mu/\rho = 50$ mm^2 s^{-1}, which agrees well with the value provided by the manufacturer. The fluid is contained in a glass syringe (500 µL,

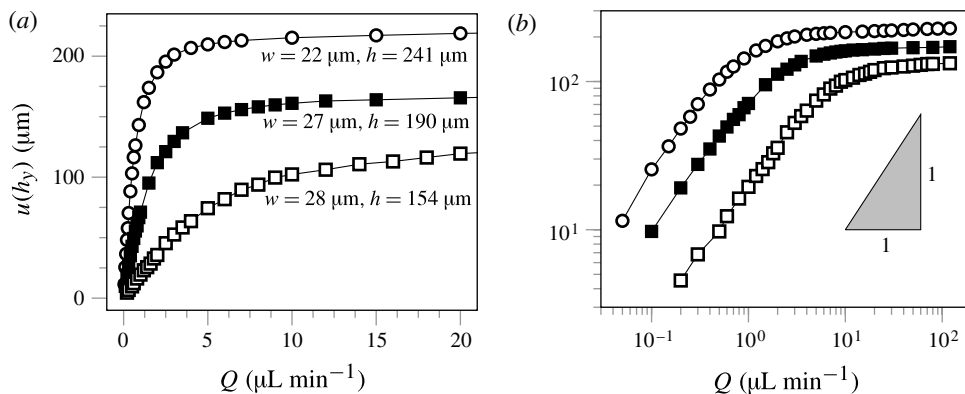FIGURE 3. (*a*) Fibre tip deflection, $u(h_y)$, versus flow rate, Q, for $d = 56\ \mu m$, $D = 66\ \mu m$, $H = 400\ \mu m$ and varying values of w and h. (*b*) The same experiments with a greater range of data plotted on logarithmic axes, which emphasize the linear trend at low flow rates.

SGE Analytical Science), and injected with a precision syringe pump (Cetoni) into the microfluidic device. The fibres are imaged at a magnification of $20\times$ (see the inset of figure 2) with the same microscope used for polymerization and a digital camera (PixeLINK) connected to a computer. The fibre deflects to a steady shape, $u(y)$, and we measure with ImageJ (NIH) the deflection at the tip, $u(h_y)$, where h_y is the y-coordinate of the centre of the fibre tip as in figure 1.

2.2. *Observations*

To gain qualitative insight into the velocity field in the channel, we seed the fluid with $2\ \mu m$ polystyrene particles (Duke Scientific) and observe the particle traces. The suspension is pumped through the device using the same set-up as for the deflection experiments, and the particles are imaged through the microscope with high-speed videography (3000 images/sec, Photron Fastcam). The resulting images are superimposed to obtain the pathlines shown in figure 2. Note that the particles are visible through the entire depth of the channel, so the image that we see is a projection of the pathlines in the z-direction. Some of the pathlines appear to pass through the fibre, while others are bent around it. The particles that appear to pass through the fibre actually flow in the thin gap above and below it, and their traces are faintly visible as the white lines on the fibre perpendicular to its axis. The balance between flow through the thin gaps above and below the fibre and flow deflected around the fibre is a defining feature of the problem. The competing confinement, and hence resistance, of flow in both directions determines this balance and influences the degree of bending of the fibre.

The focus of our paper is predicting the fibre deflection, and figure 3 shows the observed deflection versus imposed flow rate for a representative data set. A log–log plot of the data reveals that at low flow rates the deflection of the fibre tip, $u(h_y)$, is linearly proportional to the flow rate, Q. Although the current work focuses on this deflection regime, experiments were done over a wide range of flow rates extending far beyond the initial linear regime and the data is included here both for completeness and to allow us to assess how far our linearized model is valid. At the flow rates deemed to be in the linear regime (up to $Q = 1.2\ \mu L\ min^{-1}$), no deflection of the channel was observed; indeed the theory of Gervais *et al.* (2006) predicts that the

channel deformation in this flow regime is less than 1 %. The average Reynolds number, Re_D, calculated from the flow rate and channel depth, does not exceed 10^{-3} for flow rates in this regime.

3. A two-dimensional mathematical model

Before beginning we note that the full problem presented in figure 1 could be solved for individual cases using a finite-element package or a boundary integral approach. These solution methods could, in principle, capture high degrees of fibre deflection and the corresponding three-dimensional flow fields. However, we choose to use mainly analytical methods. Our solution technique fully encompasses the regime of our experiments and allows general insight into related problems. We are able to extract scalings and to obtain individual solutions through analytical and simple numerical calculations.

3.1. *Dimensional problem*

In this section we reduce the three-dimensional geometry of figure 1 to a two-dimensional flow approximation. To start with, we define the parameters of the problem using figure 1 as a guide. The dimensions of the channel are given in upper case, with height H and depth D. The volumetric flow rate is Q. For the fibre, the dimensions are given in lower case, with undeflected height h, depth d and width w. Note that h also corresponds to the total arclength of the deflected fibre, which is assumed to be inextensible. The height of the deflected fibre, projected on the y-axis, is given by h_y.

We use an Euler–Bernoulli model of beam deflection in which the fibre is approximated as being infinitely thin, with its deflection in the x-direction relative to $x = 0$ given by $u(y)$, where y ranges from 0 to h_y. If the fibre is not doubled over, the coordinate y uniquely defines a point along the fibre path. We also define a local coordinate system along the fibre path, shown in the inset of figure 1, with tangent s and normal n. For an undeflected fibre, the positive n-direction corresponds to positive x and the positive s-direction corresponds to positive y. Note that the curvilinear coordinate system is only used for derivatives; the absolute location of the fibre is described in Cartesian coordinates in order to relate it to the pressure, $p(x, y)$. The fibre curvature, $\kappa(y)$, is defined as positive in the positive n-direction.

In our analysis, the flow in the xy-plane is assumed to correspond to Hele-Shaw flow, which requires that the channel is thin and that the reduced Reynolds number is small,

$$D \ll H, \tag{3.1a}$$

$$(D/H)^2 Re_D = (D/H)^2 (\rho D v/\mu) \ll 1. \tag{3.1b}$$

From the Hele-Shaw approximation, the out-of-plane component of the velocity v_z is set to zero, while the depth-averaged velocities, $\overline{v}_x$ and $\overline{v}_y$, satisfy Darcy's law with p as the pressure,

$$\overline{\boldsymbol{v}} = (\overline{v}_x, \overline{v}_y) = -\frac{D^2}{12\mu} \boldsymbol{\nabla} p. \tag{3.2}$$

Since the flow is incompressible, $\boldsymbol{\nabla} \cdot \overline{\boldsymbol{v}} = 0$, and we obtain the Laplace equation for the pressure in the xy-plane

$$\nabla^2 p = 0, \tag{3.3}$$

with $\nabla^2 = \partial_{xx} + \partial_{yy}$. For the remainder of the paper, we shall always refer to depth-averaged velocities and write $\overline{\boldsymbol{v}} = \boldsymbol{v}$.

The velocity tends to a uniform value $v_x = Q/DH$ as $|x| \to \infty$, far away from the fibre. We integrate the momentum equation (3.2) to obtain a far-field boundary condition on pressure,

$$p \to \left(-\frac{12\mu v_x}{D^2} \right) x = \left(-\frac{12\mu Q}{D^3 H} \right) x \qquad (3.4)$$

as $|x| \to \infty$. The boundaries at the base of the fibre and the opposite wall are impermeable. Thus, to satisfy no flux at both surfaces we specify that

$$\frac{\partial p}{\partial y} = 0 \quad \text{on } y = 0, H. \qquad (3.5)$$

The pressure field is defined within an arbitrary constant, so without loss of generality we set the pressure at the tip of the fibre, $y = h_y$, to be zero,

$$p = 0 \quad \text{on } x = u(h_y) \text{ and } y = h_y, \qquad (3.6)$$

where the deflected fibre is given by $x = u(y)$.

Since the fibre only partially blocks the channel depth, some fluid can flow through the narrow gap above and below the fibre (see cross-section in the inset of figure 1 and the flow visualization shown in figure 2). Noting that the depth of the gap is $(D - d)/2$ and that the width of the gap is the width of the fibre, w, we observe for the parameters in the experiments that

$$\tfrac{1}{2}(D - d) \ll w, \qquad (3.7)$$

allowing us to use the lubrication approximation to determine the flow profile within the gap. In addition, the depth of the channel, D, and the depth of gap, $(D - d)/2$, satisfy the condition

$$\tfrac{1}{2}(D - d) \ll D, \qquad (3.8)$$

implying that the majority of the pressure drop occurs within the gap, since the resistance to flow within the gap is much higher than the resistance to flow in the main channel. This observation allows us to take the pressure on either side of the gap to be approximately constant in z but varying along the fibre length, denoted by $p_\pm(y)$, where the subscript refers to either the right- or left-hand side of the fibre, respectively.

Furthermore we require that the width of the fibre is much less than its length, or

$$w \ll h, \qquad (3.9)$$

because we approximate the fibre as an infinitely thin barrier with a certain permeability when we solve for the flow in the xy-plane. Under this approximation, the entering flux at one point on the fibre equals the exiting flux directly opposite it. Leakage dynamics that are more complex cannot be captured by a permeable barrier approximation. If condition (3.9) is met, then in the gap the resistance to flow perpendicular to the fibre is much less than the resistance parallel to the fibre, and the predominant flux through the fibre is in the perpendicular direction. Thus, the width of the fibre may be shrunk to zero while maintaining accurate leakage from the perspective of the outside flow.

The lubrication approximation is applied within the gap to relate the pressure drop across the fibre to the flow through the gap. We define the local two-dimensional flow rate perpendicular to the fibre and summed over both gaps as $q(y)$. With the height of each gap as $(D - d)/2$, the length of each gap as w and the flow rate through one gap as $q(y)/2$, the lubrication equation within one gap (either above or below the fibre) integrates to

$$\frac{p_+(y) - p_-(y)}{w} = -6\mu\, q(y) \left(\frac{2}{D - d}\right)^3. \tag{3.10}$$

By continuity, the local flow rate above and below the fibre must equal the flow rate perpendicular to the fibre (in the n-direction) immediately adjacent to it. We take the inner product of (3.2) with the vector in the n-direction to calculate the average velocity normal to the fibre, and multiply by the channel depth, D, to obtain

$$q(y) = -\frac{D^3}{12\mu} \frac{\partial p(y)}{\partial n}. \tag{3.11}$$

Thus, combining (3.10) and (3.11) yields a mixed-type (Robin) boundary condition on the pressure to be satisfied along the length of the fibre in the xy-plane,

$$p_+(y) - p_-(y) = \left(\frac{4wD^3}{(D - d)^3}\right) \frac{\partial p(y)}{\partial n} \quad \text{for } 0 < y < h_y. \tag{3.12}$$

Note that the derivative of the pressure is continuous, so it is not necessary to specify on which side of the fibre it is calculated. With boundary condition (3.12) we are no longer concerned with the specifics of the flow in the gap. Effectively, the fibre is modelled as being infinitely thin with a certain permeability governed by the coefficient linking $[p_+(y) - p_-(y)]$ to $\partial p(y)/\partial n$ in the boundary condition. In physical terms, (3.12) flattens the leakage dynamics into the xy-plane, by equating the flux entering and exiting the fibre gap to the flux through the fibre gap itself.

In deriving (3.12) we have approximated the flow as transitioning directly from Hele-Shaw flow away from the fibre to lubrication flow through the fibre itself. However, a transition region with a more complex three-dimensional velocity field must exist. For simplicity we require that the flow in this region is governed by Stokes' equations, necessitating that the Reynolds number here is small (not just the reduced Reynolds number as in (3.1b)). It is sufficient to specify this condition on the average Reynolds number calculated from the bulk flow rate and channel depth,

$$Re_D = \frac{\rho D v}{\mu} = \frac{\rho\, Q}{\mu H} \ll 1. \tag{3.13}$$

If (3.13) is satisfied then we estimate that the size of the transition region scales with the fibre depth, d (a similar idea appears in Thompson (1968)). Thus, in the transition region, a pressure drop of order $\mu v/d$ occurs and is not accounted for in (3.12). In order for our approximation to be valid we require that this additional pressure drop is small compared with both the pressure drop in the Hele-Shaw region and the pressure drop through the gap itself. A scaling argument shows that this condition may be reduced to the requirement that the depth of the channel is much less than the height of the fibre,

$$D \ll h, \tag{3.14}$$

along with inequalities (3.7) and (3.8).

To calculate the degree of bending of the fibre, we compute the force per unit length acting normal to the fibre, $f_n(y)$, by combining the pressure forces on the left and right faces, $f_p(y)$ with the viscous forces on the top and bottom faces, $f_v(y)$. The pressure is already specified and the viscous force may be found by calculating the shear stress within the gap, τ_{nz}, from the lubrication equation (3.10). Consequently,

$$
\begin{aligned}
f_n(y) = f_v(y) + f_p(y) &= \left(2\tau_{nz}w\right) - \left([p_+(y) - p_-(y)]d\right) \\
&= \left(-\frac{p_+(y) - p_-(y)}{w} \cdot \frac{(D-d)}{2}w\right) - \left(\left[p_+(y) - p_-(y)\right]d\right) \\
&= -\frac{1}{2}(D+d)\left[p_+(y) - p_-(y)\right].
\end{aligned}
\tag{3.15}
$$

The fibre is narrower than it is deep, with $w < d$, so it only deflects in the xy-plane, with no torsion. We treat the displacement of the fibre using a simplified version of the beam-bending equation that is derived in appendix A,

$$
\frac{d^2\kappa}{ds^2} + \frac{1}{2}\kappa^3 = -\frac{(D+d)}{2EI}[p_+(y) - p_-(y)],
\tag{3.16}
$$

where s is the arclength and $\kappa(y)$ is the local curvature of the fibre. The shape of the deflected fibre determines $s(y)$. The Young's modulus of the fibre is E, and the moment of inertia is

$$
I = \frac{dw^3}{12}.
\tag{3.17}
$$

Finally, to complete the problem statement four boundary conditions are required on the fibre; the end of the fibre clamped to the channel wall requires $u = du/ds = 0$ at $y = 0$, and since the fibre is slender the other end can be assumed to be moment- and shear-free, with $d^2u/ds^2 = 0$ and $d^3u/ds^3 = 0$ at $y = h_y$.

3.2. *Non-dimensional equations*

We non-dimensionalize the spatial coordinates and deflection by the channel height, H, and we scale the pressure so as to normalize the far-field condition. The scale of each variable, given in square brackets, is

$$
[x] = [y] = [s] = [n] = [u] = [\kappa]^{-1} = H \quad \text{and} \quad [p] = \frac{12\mu Q}{D^3},
\tag{3.18}
$$

and we maintain the same notation for dimensionless quantities. The non-dimensionalized y-coordinate of the tip of the deflected fibre is $c_y = h_y/H$. After algebraic steps the non-dimensional equations become

$$
\nabla^2 p = 0 \quad \text{within the cell} \tag{3.19a}
$$

$$
\frac{\partial p}{\partial y} = 0 \quad y = 0, 1 \tag{3.19b}
$$

$$
p \to -x \quad x \to \pm\infty \tag{3.19c}
$$

$$
p = 0 \quad x = u(c_y) \text{ and } y = c_y \tag{3.19d}
$$

$$
\frac{\partial p}{\partial n} = \beta(p_+ - p_-) \quad x = u(y) \text{ and } y \in (0, c_y) \tag{3.19e}
$$

$$
\frac{d^2\kappa}{ds^2} + \frac{1}{2}\kappa^3 = -\epsilon(p_+ - p_-) \quad x = u(y) \text{ and } y \in (0, c_y) \tag{3.19f}
$$

$$u = \frac{du}{ds} = 0 \qquad x = 0 \text{ and } y = 0 \tag{3.19g}$$

$$\frac{d^2u}{ds^2} = \frac{d^3u}{ds^3} = 0 \qquad x = u(c_y) \text{ and } y = c_y, \tag{3.19h}$$

with three-dimensionless parameters defining the problem,

$$\text{fibre height} \qquad c = \frac{h}{H} \tag{3.20a}$$

$$\text{permeability parameter} \qquad \beta = \left(\frac{(D-d)^3}{4wD^3} \right) H \tag{3.20b}$$

$$\text{bending parameter} \qquad \epsilon = \left(\frac{D+d}{2EI} \right) \left(\frac{12\mu Q}{D^3} \right) H^3. \tag{3.20c}$$

Not surprisingly, there are multiple ways to non-dimensionalize the distances x, y, s, n, u and κ^{-1} in (3.18): for example, one can choose the length scale so the channel height (H) is fixed or choose the length scale so the fibre height (h) is fixed. Since the focus of this paper is confinement, we choose to non-dimensionalize by H (fixing the non-dimensional channel height) and so H appears in all three of the dimensionless parameters, c, β and ϵ. This choice also isolates all effects of the fibre height to one variable, c.

For some readers, however, it might be more natural for h to appear in the bending parameter, ϵ. Had we chosen the length scale to be h (fixing the non-dimensional fibre height) the prefactor on the right-hand side of (3.19f) would contain an h^4 factor due to the second derivative of the curvature. In § 4.3, we find the proper scaling of beam deflection (non-dimensionalized by H) for small fibres, $c \to 0$, to be ϵc^5. In dimensional terms, this deflection is exactly equivalent to the h^4 scaling that would have appeared had the lengths been non-dimensionalized by h.

4. Asymptotic analysis

We focus on our experiments that are in the regime of small permeability and small deflection, so we provide an asymptotic analysis of the limit where $\epsilon \ll 1$ and $\beta \ll 1$. This analysis offers an analytical solution for the leading-order pressure field and fibre deflection, and insight into the scalings of the problem. We shall see that there are two distinguished limits depending on whether $1 \gg \beta \gg \epsilon$, referring to permeability dominated flows, or $1 \gg \epsilon \gg \beta$, referring to flexion-dominated flows.

Before continuing we note that for small deflections, $\epsilon \ll 1$, the leading-order problem can also be solved for arbitrary β, albeit numerically. For this technique, an asymptotic expansion is performed using the variable ϵ, with β left as a parameter in the problem, including at leading order. The numerical solution technique is described in § 5.2.

In this section, however, we consider an expansion of the pressure, $p(x, y)$, and deflection, $u(y)$, according to

$$p = \sum_{m=0}^{\infty} \delta^m p_m \quad \text{and} \quad u = \sum_{m=1}^{\infty} \epsilon^m u_m, \tag{4.1a,b}$$

where δ ($\ll 1$) is to be determined. At each order, p_m satisfies the Laplace equation, with impermeable walls at $y = 0$ and 1, and the reference pressure being set to zero
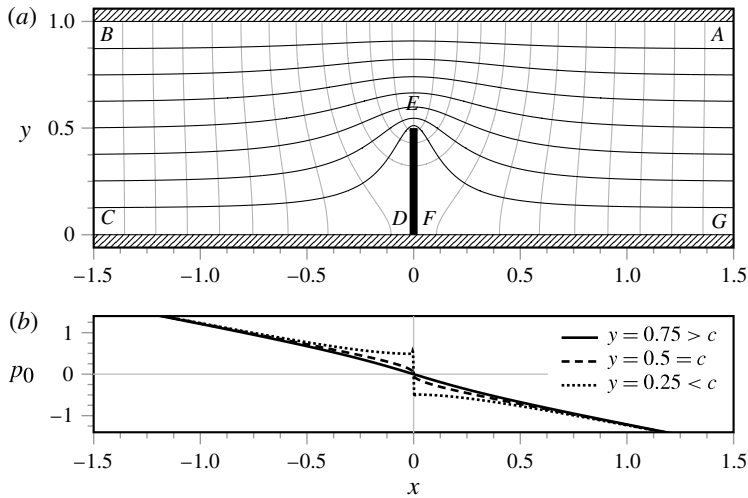
FIGURE 4. (*a*) Constant pressure curves (grey), and streamlines (black), for flow past an undeflected, impermeable fibre of length $c = 0.5$. This is the leading-order solution, p_0 and ψ_0, for flow past a lightly flexed and weakly permeable fibre. (*b*) Leading-order pressure versus x at various y heights in the channel.

at the fibre tip, as in (3.19*a*)–(3.19*d*). Owing to inextensibility, the total length of the fibre, $c = h/H$, can be related to the projected height of the fibre, c_y, through

$$c = \int_0^{c_y} \sqrt{1 + \left(\frac{\mathrm{d}u}{\mathrm{d}y}\right)^2} \, \mathrm{d}y = c_y + O(\epsilon^2), \tag{4.2}$$

so all instances of c_y in (3.19) can be replaced with c to $O(\epsilon^2)$.

At zeroth order the bending parameter $\epsilon = 0$, so the fibre is undeflected and vertical. Therefore, the leading-order geometry is symmetric about $x = 0$. We expect that the streamlines of the leading-order flow, corresponding to p_0, are also symmetric about $x = 0$, because the Laplace equation is linear in x. For reference, we show in figure 4 the leading-order streamlines and curves of constant pressure calculated using the methods of this and the following sections.

Owing to this symmetry there is no vertical component to the zeroth-order velocity in the region above the fibre, so $\partial p_0/\partial y = 0$ at $x = 0$. We integrate in y, applying the boundary condition that the pressure at the tip of the fibre is set to zero by (3.19*d*), to obtain

$$p_0 = 0 \quad x = 0 \text{ and } y \in (c, 1). \tag{4.3}$$

This condition, combined with the streamlines being symmetric about $x = 0$, requires that p_0 must be antisymmetric about $x = 0$.

Now we examine the bending equation (3.19*f*) using the expansion of (4.1*a,b*). Applying the standard definition of curvature in Cartesian coordinates, and assuming asymmetry in p_0 about $x = 0$, we see that the bending equation reduces to the usual small-deflection form,

$$\epsilon \frac{\mathrm{d}^4 u_1}{\mathrm{d}y^4} + O(\epsilon^2) = -\epsilon (p_0|_{x=0+} - p_0|_{x=0-}) + O(\epsilon\delta, \epsilon^2) \sim \mp 2\epsilon p_0|_{x=0\pm}. \tag{4.4}$$

This shows that, as expected on physical grounds, the leading- and first-order deflection is determined entirely by the zeroth-order pressure field, p_0.

Next we write the normal derivatives in the fibre permeability condition (3.19e) as

$$\left.\frac{\partial p}{\partial n}\right|_{x=u\pm} = \left[1 + \left(\frac{\mathrm{d}u}{\mathrm{d}y}\right)^2\right]^{-1}\left(\frac{\partial p}{\partial x} - \frac{\mathrm{d}u}{\mathrm{d}y}\frac{\partial p}{\partial y}\right)_{x=u\pm}. \tag{4.5}$$

Using (4.5) in the fibre condition (3.19e), and substituting the asymptotic expansions for u and p (4.1a,b), we obtain

$$\left(1 - O(\epsilon^2)\right)\left[\left(\frac{\partial p_0}{\partial x} + \delta\frac{\partial p_1}{\partial x} + O(\delta^2)\right)_{x=0\pm} + \left(\epsilon u_1 + O(\epsilon^2)\right)\left(\frac{\partial^2 p_0}{\partial x^2} + O(\delta)\right)_{x=0\pm}\right.$$
$$\left. - \left(\epsilon\frac{\mathrm{d}u_1}{\mathrm{d}y} + O(\epsilon^2)\right)\left(\frac{\partial p_0}{\partial y} + O(\delta) + O(\epsilon)\right)_{x=0\pm}\right]$$
$$= \beta\left(p_0|_{x=0+} - p_0|_{x=0-}\right) + O(\beta\delta) + O(\beta\epsilon). \tag{4.6}$$

Replacing the permeability condition on $x = u(y)$ by the expansion (4.6) about $x = 0$ is formally correct, as long as the linear beam theory of (4.4) holds, and in particular the expansion (4.1a,b) remains well-ordered. However, beam deflections that are too large may cause the series to converge slowly.

From (4.6), and with $\epsilon \ll 1$, $\beta \ll 1$, the leading-order boundary condition requires that at the fibre

$$\left.\frac{\partial p_0}{\partial x}\right|_{x=0\pm} = 0 \quad \text{at } x = 0 \text{ and } y \in (0, c), \tag{4.7}$$

which is the standard no-flux constraint. Combining the boundary conditions (4.3) and (4.7) at $x = 0$ with the boundary conditions (3.19b) at $y = 0, 1$, and (3.19c) at $x \to \pm\infty$, the p_0 problem is fully defined.

Obtaining appropriate boundary conditions for the first-order correction p_1 requires us to specify the relative magnitudes of the permeability, β, and flexion, ϵ, and this leads to three distinguished limits of (4.6).

The first limit is marked by permeability dominated effects, with $1 \gg \beta \gg \epsilon$. In this case, we choose $\delta = \beta$ in (4.6), and recalling the aforementioned symmetry of p_0, the first-order boundary condition requires that

$$\left.\frac{\partial p_1}{\partial x}\right|_{x=0\pm} = \pm 2p_0|_{x=0\pm} \quad \text{at } x = 0 \text{ and } y \in (0, c). \tag{4.8}$$

The result is a dominant balance between the horizontal gradient of p_1 and the permeability. We see that the first-order correction to the pressure field is determined by the leakage through the fibre, and is in fact independent of the deflection. Therefore, we may assume that above the straight fibre the corrected streamlines remain horizontal, so

$$p_1 = 0 \quad \text{at } x = 0 \text{ and } y \in (c, 1), \tag{4.9}$$

similar to the leading-order pressure field p_0.

The second distinguished limit is marked by flexion-dominated effects, with $1 \gg \epsilon \gg \beta$. Thus, we choose $\delta = \epsilon$, and the first-order boundary condition requires

at $O(\epsilon)$ that

$$\frac{\partial p_1}{\partial x}\bigg|_{x=0\pm} = \left(\frac{\mathrm{d}u_1}{\mathrm{d}y}\frac{\partial p_0}{\partial y} - u_1\frac{\partial^2 p_0}{\partial x^2}\right)_{x=0\pm} \quad \text{at } x = 0 \text{ and } y \in (0, c). \quad (4.10)$$

We see here that an advective flux around the deflected fibre leads to the gradient in p_1. In order to apply this boundary condition, the deflection, $u_1(y)$, must first be computed using (4.4).

The third distinguished limit is marked by equal magnitudes of permeability and flexion, with $\delta = \epsilon = O(\beta)$, and the boundary condition on $\partial p_1/\partial x$ is the sum of (4.9) and (4.10). The linearity of the asymptotic approximation then implies that the solutions of the permeability and flexion dominated limits can be independently superimposed to form a solution of the third type.

It is worthwhile to note that for a given channel and fibre geometry, all three distinguished limits may be reached by varying the flow rate, Q. Since ϵ is the only term that contains Q, and ϵ is proportional to Q, it should be possible, starting with low Q and increasing, to satisfy in a sequential manner the conditions that $\epsilon \ll \beta$, $\epsilon = O(\beta)$, and $\epsilon \gg \beta$. In other words, if the flow rate in an experiment is gradually increased from a very low value, the first-order pressure correction will transition from being permeability-dominated to flexion-dominated.

4.1. *The leading-order pressure, p_0*

The leading-order pressure, p_0, consists of potential flow through a finite channel past a infinitely thin, impermeable fibre. In solving for the potential flow contained within an impermeable boundary, complex variable methods known as conformal mapping can be used to determine analytic solutions in certain cases. These methods rely upon mapping the physical geometry to an alternate and simpler geometry (such as a disc or upper half-plane) where the problem is hopefully tractable. Once this new problem is solved, inverting the map produces the solution in the original geometry. For a description of such methods, see reviews by Milne-Thomson (1968) and Ablowitz & Fokas (2003).

The case of flow past a thin, vertical barrier in an unconfined, upper half-plane is well-known as a standard exercise in conformal mapping (Ablowitz & Fokas 2003, p. 355). We have found that an explicit formula can be written for the confined geometry as well. The method begins by noting that since p_0 satisfies the Laplace equation, we can first define the complex potential

$$w_0(z) \equiv p_0(x, y) + \mathrm{i}\psi_0(x, y), \quad (4.11)$$

where ψ_0 is the stream function and harmonic conjugate of p_0, and $z = x + \mathrm{i}y$. Note that w_0 satisfies the Laplace equation, and all of the solid boundaries are impermeable to leading order. In our method, the physical z-plane (figure 4) is first mapped to the potential w_0-plane (figure 5a, maintaining labels A–G). In particular, the tip of the barrier ($z = \mathrm{i}c$), is mapped to $w_0 = 0$ because of condition (4.3), while the two stagnation points are located at $w_0 = \pm k$. The value k is currently unknown, and corresponds to the barrier 'length' in the potential plane.

Next, the w_0-plane is mapped to the upper-half ζ-plane (figure 5b). To simplify calculations, we choose to map point F to $\zeta = 1$, and solve for ζ_E and ζ_D later; the transformation is then

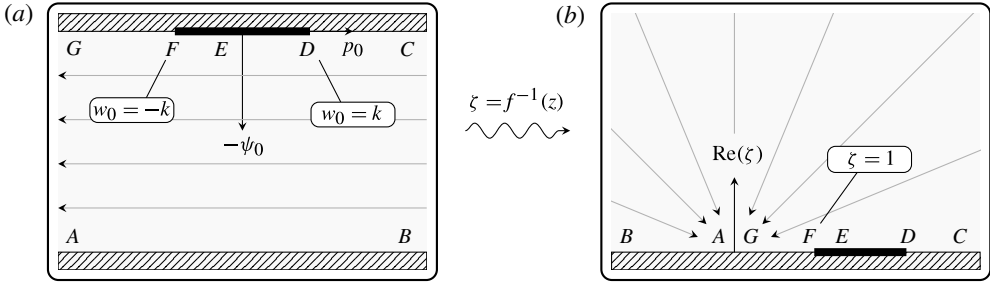$$\zeta = \zeta_E \mathrm{e}^{\pi w_0}. \quad (4.12)$$

FIGURE 5. The physical z-plane is mapped to (a) the potential w_0-plane and then to (b) the upper-half ζ-plane. In the potential plane, streamlines (grey) run parallel to the p-axis, while in the ζ-plane, streamlines (grey) are generated by a sink at $\zeta = 0$.

Now, the goal is to provide a map from the z-plane to the ζ-plane, after which the pressures and velocities follow from (4.12). The Schwarz–Christoffel formula provides this connection (cf. Milne-Thomson 1968), and for this particular problem it is given by

$$z = f(\zeta) \equiv K \int_1^\zeta \frac{(\zeta' - \zeta_E)}{\zeta'\sqrt{(\zeta' - \zeta_D)(\zeta' - 1)}} \, d\zeta'. \tag{4.13}$$

The symmetry in the potential plane implies that $\zeta_D = \zeta_E^2$, and the constant K can be derived by requiring that the velocity upstream satisfies $dw_0/dz = -1$, or simply that

$$\pi\zeta \frac{dz}{d\zeta} = \pi\zeta \frac{K}{\zeta} = -1, \tag{4.14}$$

giving $K = -1/\pi$. The integral (4.13) can now be computed in closed form and yields

$$z = f(\zeta) = \frac{1}{\pi} \log \left(\frac{\zeta \left(-1 + \zeta_E^2\right)^2 \left(2\zeta_E^2 - \zeta_E - \zeta\zeta_E^2 - 2\zeta_E\sqrt{(\zeta - 1)(\zeta - \zeta_E^2)}\right)^{-1}}{1 - 2\zeta + \zeta_E^2 + 2\sqrt{(\zeta - 1)(\zeta - \zeta_E^2)}} \right), \tag{4.15}$$

where we have selected the principle branch of the square roots and logarithm.

In order to solve for ζ_E, we now impose the barrier condition, $f(\zeta_E) = ic$. Owing to the branch structure of (4.15), two solutions are given, but the relevant one is

$$\zeta_E = \left(\frac{1 + \sin(c\pi/2)}{1 - \sin(c\pi/2)} \right). \tag{4.16}$$

Note that the barrier sizes in the physical and potential planes are now related through $\zeta_E = e^{-\pi k}$. It remains to invert (4.15), which can be simplified to

$$\zeta = f^{-1}(z) = A(z) - B(z)\sqrt{\Delta(z)}, \tag{4.17a}$$

while taking the principal branch of the square root, and with components given by

$$\Delta(z) = (1 - e^{\pi(z+ic)})(1 - e^{\pi(z-ic)}) \tag{4.17b}$$

$$A(z) = \frac{1 - \cos(c\pi) + 2\cosh(\pi z)}{2[1 - \sin(c\pi/2)]^2} \tag{4.17c}$$

$$B(z) = -\frac{(e^{-\pi z} + 1)}{2[1 - \sin(c\pi/2)]^2}. \qquad (4.17d)$$

The complex potential can now be determined from (4.12), or

$$w_0(z) = \frac{1}{\pi} \log\left(\frac{\zeta}{\zeta_E}\right) = \frac{1}{\pi} \log\left[f^{-1}(z)\left(\frac{1 - \sin(c\pi/2)}{1 + \sin(c\pi/2)}\right)\right], \qquad (4.18)$$

with the pressure $p_0(x, y) = \text{Re}(w_0)$. Curves of constant pressure and streamlines are shown in figure 4 for a fibre of length $c = 0.5$.

In computing (4.17), care must be exercised with regards to the branch structure. In particular, the square root of (4.17b), which appears in (4.17a), contains branch points at $z = \pm i(c + 2\pi m)$ for $m \in \mathbb{Z}$. These are manifestations of the discontinuity caused by the barrier and the easiest way to compute (4.17) is to take the branch cut at $z = ic$ directly down the imaginary axis and all other branch cuts parallel to the horizontal axis. This step allows the use of (4.17) throughout the physical channel without changing branches.

Possessing a closed-form solution for the leading-order problem is valuable for several reasons. First, the asymptotics in the two limits of small and large fibres are derived easily. Deriving higher-order approximations for flows with asymptotically small geometries is not a trivial problem (see, for example, Tuck 1964), and an explicit solution can be used to work backwards to derive the subdominant contributions. Second, the numerical computations in § 5 are less intensive computationally once the most singular impermeable behaviour has been subtracted out.

4.2. *The small fibre limit* ($c \to 0$)

In the limit that $c \to 0$, the flow in the outer region, with $x, y = O(1)$ fixed and independent of c, simply tends to uniform flow. From the exact solution (4.18), we can expand for an outer solution

$$w_{0,out} = -z - \left(\frac{\pi}{4}\coth\left(\frac{\pi z}{2}\right)\right)c^2 + O(c^4). \qquad (4.19)$$

The outer solution does not satisfy the fibre permeability condition given by (4.7) to leading order, $\frac{\partial p_0}{\partial x} = 0$, so we search for an inner region where the appropriate scaling is

$$z = cZ \quad \text{and} \quad w_0 = c\,W_0. \qquad (4.20a,b)$$

Within the inner region, the problem for W_0 consists of solving for potential flow in the upper-half Z-plane, with an impermeable slit along $0 < Y < 1$. From the exact solution we have

$$W_0 = -\sqrt{Z^2 + 1} - \left(\frac{\pi^2}{24}\sqrt{Z^2 + 1}\right)c^2 + O(c^4), \qquad (4.21)$$

for which the leading-order term can be seen to match the uniform flow as $|Z| \to \infty$. In fact, this term is simply the solution for flow past a barrier of length one in a semi-infinite plane, and can be derived in the usual way using conformal mapping (cf. Ablowitz & Fokas 2003, p. 355). We may combine (4.19)–(4.21) in order to form a uniformly valid solution $w_{0,unif} \sim -\sqrt{z^2 + c^2}$, corresponding to a pressure field

$$p_{0,unif}(x, y) \sim -\text{Re}\left(\sqrt{(x + iy)^2 + c^2}\right). \qquad (4.22)$$

4.2.1. *Pressure field for large fibres* ($c \to 1$)

If we write $\gamma = (1 - c)$ and take the limit of large fibres, $c \to 1$, so that $\gamma \to 0$, then at leading order we have flow through a small slit which produces a unit flux. Away from the slit, and in a region where x and $1 - y$ are $O(1)$, we have from (4.18) an expansion for the potential,

$$w_0 = \frac{2}{\pi} \log \gamma - \frac{1}{\pi} \log \left[\frac{8}{\pi} (1 + \cosh(\pi z)) \right] + O(\gamma^4). \tag{4.23}$$

The first term indicates that the pressure is logarithmically divergent everywhere within $O(1)$ distances in the bulk of the flow, and the second term corresponds to the problem of flow produced in a channel due to a source or sink at a point along the channel wall (cf. Milne-Thomson 1968, p. 272). However, there are two relevant regions where the approximation in (4.23) breaks down and these regions are marked by locations where the second term becomes of the same order of magnitude as the first.

There is an inner region near the slit where the relevant inner variable, Z, is defined through $z = i[1 - (1 + Z)\gamma/2]$, with an inner solution $w_{0,in} = -\log[\pi(1 + Z)^2]/\pi + O(\gamma^2)$, and a corresponding inner pressure field

$$p_{0,in} = -\frac{1}{\pi} \mathrm{Re} \left(\log \left[\frac{4\pi}{\gamma^2} (1 + ix - y)^2 \right] \right) + O(\gamma^2). \tag{4.24}$$

This inner solution indeed satisfies the tip condition $w_{0,in} = 0$ as $Z \to 0$, and as $Z \to \infty$ it reproduces the source term seen in (4.23). In addition to the inner scaling, there is a far-field scaling in (4.23), which is required in order to match the uniform flow. This occurs when $z = O(\log \gamma)$, and the second term in (4.23) becomes of leading order.

4.3. *Predictions of tip deflection*

Having derived the leading-order approximation of the potential, w_0, which yields the leading-order pressure field, we may now integrate the Euler–Bernoulli equation (4.4) four times to obtain the deflection of the beam. Once the boundary conditions at the bottom and top of the fibre are imposed, the expression becomes

$$u(y) \sim \epsilon \int_0^y \int_0^{y_4} \int_c^{y_3} \int_c^{y_2} 2p_0(x = 0_-, y_1) \, \mathrm{d}y_1 \, \mathrm{d}y_2 \, \mathrm{d}y_3 \, \mathrm{d}y_4, \tag{4.25}$$

with the lower limits of integration having been chosen to satisfy the boundary conditions automatically. For small fibres, the pressure along the left-hand side of the fibre is $p_0 \sim \sqrt{c^2 - y^2}$ from (4.22). Integrating this function in (4.25), we obtain an expression for the maximal deflection for $c \ll 1$,

$$u(c) \sim \epsilon c^5 \left(\frac{\pi}{16} - \frac{2}{45} \right) \simeq 0.15 \, \epsilon c^5. \tag{4.26}$$

In the large fibre limit discussed in §4.2.1, with $c \to 1$, the pressure is logarithmically large on the scale of the fibre. Using (4.23), we find that the deflection of the fibre tip is governed by

$$u(c) \sim \epsilon \left(-\frac{1}{2\pi} \log(1 - c) + \Lambda \right), \tag{4.27}$$
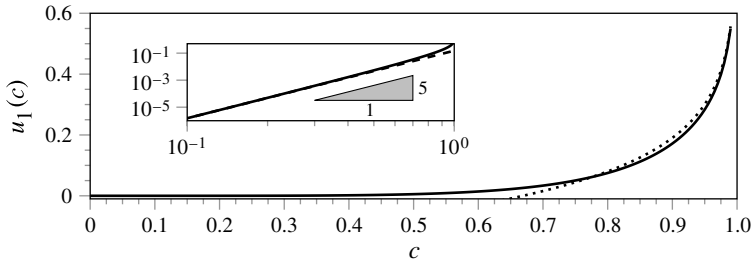
FIGURE 6. The solid line represents the deflection of the fibre tip, $u_1(c) \sim u(c)/\epsilon$, calculated from (4.25) using the full solution of p_0. As $c \to 1$, $u_1(c)$ diverges logarithmically according to (4.27), shown as a dotted line. In the inset the full solution is again plotted as a solid line, and the $c \to 0$ limit from (4.26) is shown dashed.

where the constant is numerically determined to be $\Lambda \approx -0.176$. The solutions $u/\epsilon \sim u_1$, are shown in figure 6. At large and small c the analytical limits, (4.26) and (4.27), closely approximate the full solution (4.25).

Effectively, (4.26) implies that within the small fibre limit, the correct scale of deflection is $O(\epsilon c^5)$ instead of $O(\epsilon)$. Consequently, as $c \to 0$, ϵ is allowed to be quite large (i.e. $\epsilon \ll 1/c^5$), rather than the more strict $\epsilon \ll 1$. Thus, in this limit the fibre can be allowed to be increasingly flexible and the flow rate can be increasingly high without violating the requirements of the linearized theory. Furthermore, because of the c^5 dependence, in order to match the observed $O(1)$ deflections in the experiments (where $c \approx 0.3$–0.8), ϵ must in fact be quite large. In the case of large fibres, $c \to 1$, however, the bending parameter must satisfy the rather stringent requirement of $\epsilon \ll 1/|\log(1-c)|$. If the fibre is too large, the theory breaks down unless the fibre is kept sufficiently stiff or the flow rate is kept sufficiently low.

4.4. *Predictions of leakage*

We can also develop an approximation for the amount of fluid flowing through the fibre, which can be measured using the horizontal velocity at $x = 0$. The velocity is proportional to the pressure gradient, and as we showed in (4.8) and (4.10), the pressure gradient depends on the relative balances of permeability and fibre bending, and can be described in the two limits as

$$v_x/\beta \sim \mp 2p_0|_{x=0\pm} \quad \text{for } \beta \gg \epsilon \tag{4.28}$$

$$v_x/\epsilon \sim -\left(\frac{\mathrm{d}u_1}{\mathrm{d}y}\frac{\partial p_0}{\partial y} - u_1\frac{\partial^2 p_0}{\partial x^2}\right)_{x=0\pm} \quad \text{for } \epsilon \gg \beta, \tag{4.29}$$

where v_x is scaled by the average velocity in the channel, Q/DH. From (4.28), we see that when the leakage at the fibre is primarily due to permeability, i.e. $\beta \gg \epsilon$, the largest leakage occurs near the origin at the base of the fibre where the pressure is maximal. The least leakage is near the fibre tip where the pressure is zero. In contrast, when fibre flexion governs v_x, i.e. $\epsilon \gg \beta$ in (4.29), then the local leakage is zero at the fibre base and large at the fibre tip. At the tip, the second derivative of the leading-order pressure is infinite and the fibre is bent, allowing the fluid to pass. Both results are plotted in figure 7.

There is one unusual element of the horizontal velocities. Recall that p_0 is antisymmetric, so for $\beta \gg \epsilon$, we see from (4.28) that the velocity is both continuous and positive at the fibre as expected. However, for $\epsilon \gg \beta$, we can verify that the
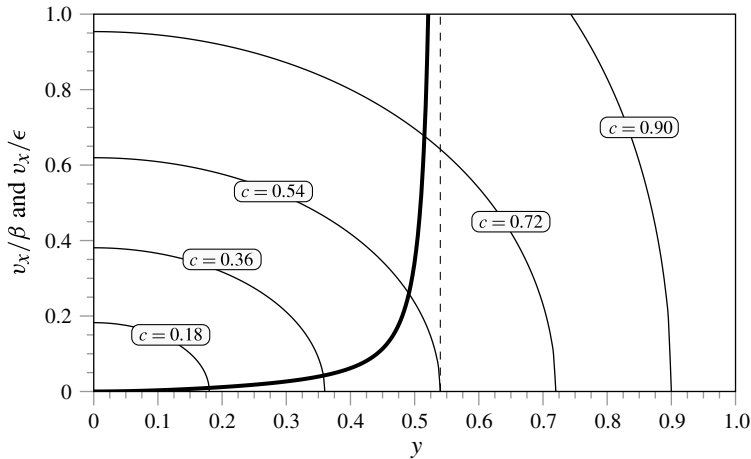
FIGURE 7. The leading-order horizontal velocity, v_x/β, at $x = 0_\pm$ for permeability dominant flows, $\beta \gg \epsilon$ (shown thin). Also plotted is the horizontal velocity, v_x/ϵ, at $x = 0_-$ for a flexion dominated flow, $\epsilon \gg \beta$, with fibre length $c = 0.54$ (shown bold). The horizontal velocity at $x = 0_+$, for $\epsilon \gg \beta$, is the negative of the plotted value.

velocity in (4.29) is positive on the left, but negative on the right. Thus, the asymptotic approximations predict a flow rightwards on the left of the fibre, but leftwards on the right. This is counterintuitive because for any non-zero amount of deflection (and hence any $\epsilon > 0$), we would expect the flow at the origin to be both continuous and positive.

In fact, this peculiarity in our asymptotics is due to a further distinguished limit in the process of taking both $x \to 0_+$ and $\epsilon \to 0$. Note that in our methodology (cf. in particular (4.10)), we first took $\epsilon \to 0$, projected the fibre onto the axis $x = 0$, and only then took the limit of $x \to 0$. This, however, is different from taking $x \to 0_+$ first (to where the fluid is continuous and has positive horizontal velocity), followed by taking $\epsilon \to 0$.

We clarify this issue in appendix B. There, the conclusion is that there exists a curved region of $O(\epsilon)$ near the fibre where the asymptotic approximation (4.10) is invalid. The asymptotic series of (4.1*a,b*) should then be interpreted as an outer approximation to be matched to an inner solution near the fibre. However, because the inner limit of the outer solution is known to all orders by (4.6), the solution in the inner region is unimportant as far as the general macroscopic flow is concerned; it only serves to explain why the velocity on the right of the fibre predicted by (4.10) is negative rather than positive.

5. Numerical results

In this section we present numerical computations for the first-order pressure, p_1, of §4. In addition, we present a numerical method for solving the system of equations (3.19) with arbitrary degrees of permeability. An eigenvalue decomposition at $x = 0$ is used to calculate p_1 in the permeability dominated case ($1 \gg \beta \gg \epsilon$), and for the case of arbitrary permeability ($\beta = O(1)$, $\epsilon \ll 1$). However, when flexion dominates ($1 \gg \epsilon \gg \beta$), the p_1 calculations necessitate a global scheme, and the difficulties of
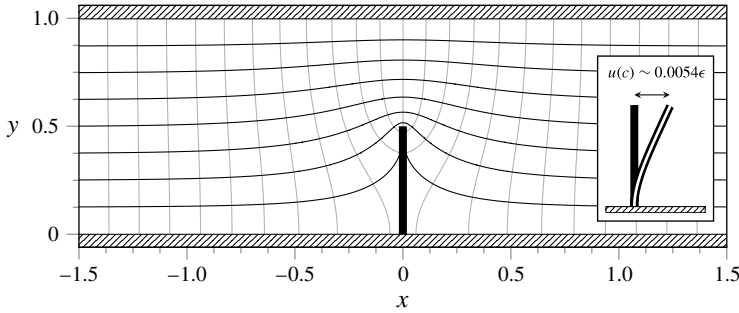
FIGURE 8. Streamlines (black), and constant-pressure curves (grey), both given in increments of 0.125, of $p = p_0 + \beta p_1$ for the permeability-dominated case $\beta \gg \epsilon$ where $\beta = 0.3$. The fibre length is $c = 0.5$, and the inset plot shows the leading-order deflection of the fibre, $u \sim \epsilon u_1$.

such a scheme are discussed. A coupled finite-element package may be appropriate for this case.

5.1. *Permeability dominated flows* ($\epsilon \ll \beta \ll 1$)

In flows where the permeability dominates, the majority of the flux past the fibre in the three-dimensional problem can be attributed to the flow of fluid going through the gap above and below the fibre, rather than due to the fibre bending. The object is to calculate $p_1(x, y)$ subject to satisfying the Laplace equation within the channel, no-flux conditions at the upper and lower walls, with $p_1 \to 0$ as $|x| \to \infty$, and the conditions (4.8) and (4.9) at $x = 0$. We expand p_1 into a truncated Fourier series with M modes

$$p_1(x, y) = \frac{b_0}{2} + \sum_{m=1}^{M-1} b_m e^{-m\pi|x|} \cos(m\pi y), \tag{5.1}$$

with eigenfunctions chosen so as to satisfy all conditions on p_1 except for those at $x = 0$. The unknown coefficients b_m are then obtained by imposing the two boundary conditions along $x = 0$,

$$\sum_{m=1}^{M-1} (m\pi) b_m \cos(m\pi y) = -2 p_0(x = 0_-, y) \quad \text{for } 0 \leqslant y < c, \tag{5.2a}$$

$$\frac{b_0}{2} + \sum_{m=1}^{M-1} b_m \cos(m\pi y) = 0 \quad \text{for } c \leqslant y < 1, \tag{5.2b}$$

where p_0 is computed using (4.18).

The theory of mixed boundary value problems, studied using a dual series formulation such as this, is discussed by Sneddon (1966). We solve for the coefficients b_m using collocation: we distribute M points along the interval, $y \in [0, 1]$, and solve the resultant $M \times M$ system of equations using Newton's method. In general, the solution converges rapidly, and only a modest number of uniformly distributed mesh points are required ($M = 50$ for most computations).

In figure 8, the streamlines of the two-term approximation, $p \sim p_0 + \beta p_1$ are drawn for the case of permeability dominated flows with $\beta = 0.3$. The ability for the model to capture a small degree of leakage past the fibre is evident. We have chosen a

relatively large value of β simply to emphasize the influence of leakage, and the first-order streamlines (p_1-streamlines) clearly show passage through the fibre. As β tends to zero, the majority of the streamlines that pass through the fibre are seen to be localized near the origin. At this point, v_x/β given in (4.28) is maximized and the first-order contribution is sufficiently large to divert the flow through the fibre, rather than simply around the structure.

5.2. *Small deflection of fibres with arbitrary permeability* ($\epsilon \ll 1$, $\beta = O(1)$)

Although up to now our analysis has been focused on the limit of small permeability, our model in (3.19) is also valid for arbitrary permeability. If we let $\beta = O(1)$ but keep $\epsilon \ll 1$, then we can treat the problem using the boundary perturbation method only, expanding p and u explicitly in terms of ϵ as $p = p_0 + O(\epsilon)$ and $u = \epsilon u_1 + O(\epsilon^2)$. We emphasize that in this new asymptotic framework the leading-order pressure, p_0, and deflection, u_1, both include effects of permeability.

Since we are still concerned with small deflections, p_0 is again assumed to be antisymmetric about $x = 0$. This allows us to extend the condition of $p_0 = 0$ throughout the gap $y \in (c, 1)$ at $x = 0$, as in §4. The boundary condition at the fibre (3.19e) becomes at leading order

$$\left.\frac{\partial p_0}{\partial x}\right|_{x=0\pm} = 2\beta p_0|_{x=0+} = -2\beta p_0|_{x=0-}, \tag{5.3}$$

and to solve for p_0 we choose to write,

$$p_0 = \phi + \tilde{p}_0. \tag{5.4}$$

where we have separated p_0 into an approximate solution ϕ and a correction $\tilde{p}_0$.

When β is small and the bulk of the fluid is deflected around the fibre, we take ϕ to be the leading-order impermeable solution in §4.1. However, if β is larger, and particularly in the limit that $\beta \to \infty$, the boundary condition along the fibre becomes $p_0 \to 0$ at $x = 0$, and we expect that the fluid completely passes through the fibre; the leading-order approximation suggests that we choose $\phi = -x$.

In either case, if we use the Fourier series representation of (5.1) for $\tilde{p}_0$, the boundary condition at the fibre (5.3) becomes

$$(-2\beta)\frac{b_0}{2} + \sum_{m=1}^{\infty}(-m\pi - 2\beta)b_m\cos(m\pi y) = 2\beta\phi - \frac{\partial\phi}{\partial x} \quad \text{for } 0 \leqslant y < c, \tag{5.5}$$

and is combined with (5.2b) for $c \leqslant y < 1$. The right-hand side of (5.5) is evaluated as $x \to 0_-$, and is equal to one when we choose $\phi = -x$.

The equation for the deflection is the same as (4.4) and the leading-order deflection u_1 is numerically integrated with (4.25). We emphasize again that in this case p_0 contains effects of leakage and therefore the prediction u_1 is based on leakage effects as well. An example of the numerical computation of p_0 and u_1 is shown in figure 9 with permeability $\beta = 2$ and fibre length $c = 0.5$. It should be apparent that the large value of β has allowed the fluid to pass nearly unhindered by the fibre, and thus the streamlines closely approximate those for uniform flow.

5.3. *Flexion-dominated effects* ($\beta \ll \epsilon \ll 1$)

Returning to the asymptotic formulation presented is §4, we examine the first-order correction to the pressure field in the flexion-dominated regime. The difficulty of numerical computations in this regime is that we no longer know the value of p_1
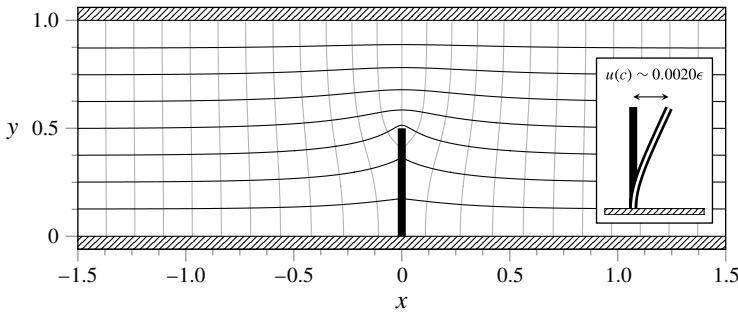
FIGURE 9. Streamlines (black) and constant pressure lines (grey), both given in increments of 0.125, of the numerical solution for $\beta = O(1)$ and $\epsilon \ll 1$ from § 5.2. The fibre length is $c = 0.5$ and permeability $\beta = 2$. The inset plot shows the leading-order deflection of the fibre, $u \sim \epsilon u_1$.

on $x = 0$ and $c < y < 1$ (cf. for comparison (5.2b)). Thus, the dual series approach, which effectively reduces the two-dimensional problem in the channel to a one-dimensional problem along $x = 0$, no longer applies for this case.

Numerical computations in this regime require a global method. For example, we may attempt to compute p_1 using a boundary integral approach (see, for example, Pozrikidis 1992; Vanden-Broeck 2010). However, there is a significant difficulty towards implementing this approach (and, indeed, any global solver): from the discussion in § 4.3, we know that the normal derivative of p_1, given by (4.10), contains a non-integrable singularity at the point $(0, c)$. In fact, our asymptotic analysis in § 4 can be used to simplify these numerical schemes by allowing us to remove the dominant singularity at the fibre tip. However, implementing these numerical methods would take us beyond the scope of this paper, and we have chosen to leave such a scheme to future work.

6. Discussion

To assess the validity of the leading-order model presented in this work, we may compare the predictions of fibre deflection to the experimental observations of § 2. The basis of our theoretical treatment is that the small deflection follows $u \sim \epsilon u_1$, and we showed how to calculate u_1 as a function of the dimensionless fibre height $c = h/H$ using (4.25), i.e. $u_1(c)$. Substituting the definitions of dimensionless u (3.18) and ϵ (3.20c) into the asymptotic form, $u \sim \epsilon u_1$, we can write the dimensional deflection u as

$$u \sim \left[\frac{6\mu(D+d)H^4 Q}{EID^3} \right] u_1(c), \tag{6.1}$$

which gives a prediction for the slope of u versus Q, for small Q. We now rearrange this equation to compare physical quantities on the right to a calculated quantity, $u_1(h/H)$, on the left and obtain

$$u_1(c) \sim \left[\frac{E\left(\frac{1}{12}dw^3\right)D^3}{6\mu(D+d)H^4} \right] \frac{u}{Q}, \tag{6.2}$$

where we have substituted I from (3.17). Thus, u_1 is essentially a scaling of u/Q, and should collapse the data for different geometries (different w) so that it is only a function of $h/H = c$.
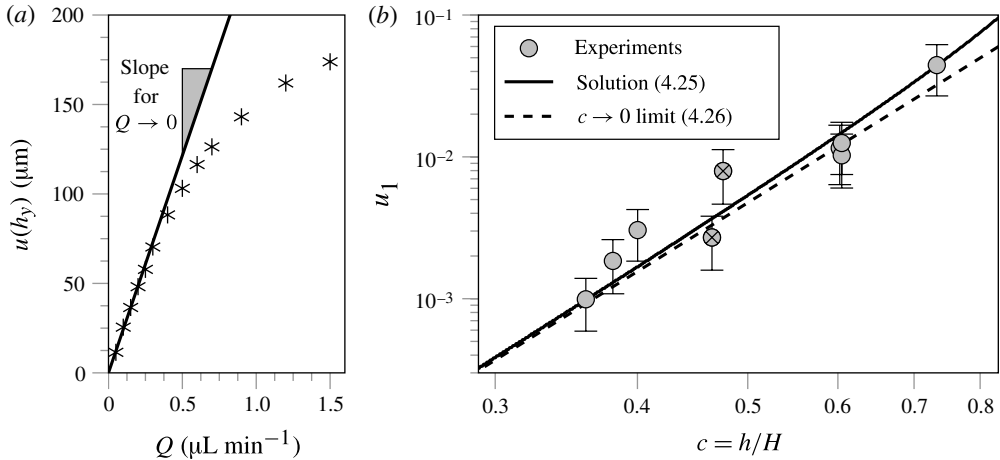
FIGURE 10. (*a*) Experimental deflection data measured from one particular fibre, with $w = 22 \, \mu m$, $h = 241 \, \mu m$, $d = 56 \, \mu m$ and $D = 66 \, \mu m$. The solid line represents the slope of u versus Q as $Q \to 0$ for this fibre, fitted from the first five data points. (*b*) Data points show values of u_1 for all experiments (determined from measured u/Q and average E), along with theoretical predictions given by solid and dashed lines. In the experiments w varies from 22 to 34 μm, but the form of u_1, (6.2), scales out this dependency. The horizontal error bars are smaller than the data points. The two middle points are crossed to highlight them for discussion in the text. Values of β lie between 0.0179 and 0.0226.

6.1. *Comparison with experiments*

We now seek to validate (6.2): first, we determine the initial slope u/Q for an individual fibre from the recorded deflection data by fitting a least-squares linear regression to the data points at low flow rates. One data set, with its linear regression, is shown in figure 10(*a*).

Now all terms in (6.2) are known except for the Young's modulus, E. Most importantly, we know the ratio $c = h/H$, and therefore we may calculate a prediction for $u_1(c)$ using (4.25). We thus solve for the unknown E in (6.2) for each experiment, using the measured slope u/Q and the prediction $u_1(c)$. We then average E over all experiments to obtain $E = 63 \pm 22$ kPa. An additional benefit of this experimental set up then is that it allows us to measure the elasticity of PEGDA polymerized with these specific cross-linking conditions, which we believe had not been done before.

We may now determine experimental values of u_1 from the expression on the right-hand side of (6.2), using the average value of $E = 63$ kPa and the measured values of u/Q, w, d, D, H and μ. Note that, since the average value of E is used for all experiments, the effect of E is only to offset all data points by a multiplicative constant; the shape of the $u_1(c)$ trend is unaffected. Recall that w varies from 22 to 34 μm, and that h varies from 144 to 293 μm; all other parameters are held constant. All experimental values of u_1 are plotted as a function of c in figure 10(*b*), with the dependency on w scaled out through (6.2).

The leading-order solution $u_1(c)$, computed using (4.25), is shown alongside the data in figure 10*b* for comparison. The analytical solution for small c, given by (4.26), is presented as well. Error bars in the plot are determined from estimated variances in the parameters involved in calculating u_1, as well as the variance in E reported above

and the error in calculating the regression for the initial slope of u versus Q (Student's t test, with 95 % confidence interval). The permeability parameter, β, ranges from 0.0179 to 0.0226, and since β is small we expect the experimental values of u_1 to lie close to the leading-order solution.

Indeed, the data appears to agree well with the trend $u_1(c)$ calculated from (4.25), although there exists some scatter. We can posit various reasons for the observed scatter, with perhaps the most likely being variations in fibre elasticity. Great care was taken to ensure constant polymerization conditions, but this is a relatively new experimental technique, and reproducibility issues have been raised before (Berthet 2012). The Young's modulus E could vary from fibre to fibre and we have no direct way of measuring this on a specific fibre; instead we average over the suite of experiments to obtain a value of the Young's modulus with variances. Variations in Young's modulus are most apparent in the two 'crossed' data points in figure 10*b*. The geometry of these experiments is nearly identical, but they lie on opposite sides of the predicted trend, indicating the presence of some unobservable difference between the two fibres. Another possible reason for the scatter is difficulty in measuring the fibre depth, d.

The model is able to predict the deflection within reasonable error bounds for much of the dataset, however, and this resolution is likely good enough for one application of our technology: microfluidic flow measurement. Given a microfluidic channel of a certain geometry and a microscope capable of sensing deflections at a certain resolution, our model can be used to specify the size of the sensing fibre necessary for a range of expected flow rates. Then, as long as the flow remains in the linear regime, only one calibration experiment is necessary to precisely calibrate flow measurement.

7. Conclusion

In this paper we have presented an experimental and theoretical study investigating the dynamics of confined fibres bent by an external viscous flow. Using a novel microfluidic setup, we constructed flexible micrometre-sized fibres anchored in a channel and performed experiments measuring tip deflection versus flow rate. We proposed a mathematical model that reduced the three-dimensional geometry of the flow to a two-dimensional Hele-Shaw approximation. Within the two-dimensional approximation, boundary conditions at the fibre allowed for leakage flow through the small gap above and below the fibre, giving the confined fibre an effectively permeability.

Motivated by the experimental observation of a linear relationship between deflection and flow rate for highly confined fibres at low flow rates, asymptotic solutions were sought in the limits of small flexion (ϵ) and small permeability (β). The leading-order pressure field, p_0, was derived in closed form using complex variable methods. It was shown that there exist two distinguished limits for the first-order pressure correction, p_1, and results for these two limits are summarized in table 1. A similar problem formulation was then used to numerically solve for the pressure field corresponding to arbitrary degrees of dimensionless permeability, β.

We use the leading-order pressure field, p_0, to predict the leading- and first-order deflection of the fibre, and validate our calculations with analytical limits at small and large fibre heights. The predicted deflection compares favourably to the results of our microfluidic experiments and allows us to measure the elasticity of PEGDA polymerized with our specific cross-linking conditions. We note that there still exist open questions to be studied with the tools presented in this paper. Further work could

	Permeability dominated $1 \gg \beta \gg \epsilon$	Flexion dominated $1 \gg \epsilon \gg \beta$
Correction to flow streamlines	Symmetric about $x = 0$	Lacks symmetry due to fibre deflection
Location of maximum flux at $x = 0$	Fibre base	Fibre tip
Numerical solution method	Dual Fourier series along centreline $x = 0$	Global method (e.g. boundary integral)

TABLE 1. Properties of the first-order pressure correction, p_1.

be done investigating the regime of large fibre deflections, the dynamics of a system with multiple fibres, and the effects of channel elasticity.

Acknowledgement

Appendix A. Derivation of beam bending equation

In this appendix we derive the simplified beam bending equation (3.16). We define the force per unit length acting on a fibre as $\boldsymbol{f} = f_s \boldsymbol{e}_s + f_n \boldsymbol{e}_n$ and the force and moment transmitted through the fibre as $\boldsymbol{T} = T_s \boldsymbol{e}_s + T_n \boldsymbol{e}_n$ and M, respectively. The unit vectors $\boldsymbol{e}_s$ and $\boldsymbol{e}_n$ are in the tangential and normal directions. We perform a force and moment balance on an infinitesimal section of the fibre, while specifying inextensibility, to obtain

$$\frac{\mathrm{d}\boldsymbol{T}}{\mathrm{d}s} + \boldsymbol{f} = \boldsymbol{0} \quad \text{and} \quad \frac{\mathrm{d}M}{\mathrm{d}s} + T_n = 0. \qquad (\text{A } 1a,b)$$

Assuming that the moment is tied to the curvature through $M = EI\kappa$, we arrive at a set of equations to describe the deflection of the fibre through a balance of forces in the two directions,

$$\boldsymbol{e}_s \text{ component}: \quad \frac{\mathrm{d}T_s}{\mathrm{d}s} + EI\kappa \frac{\mathrm{d}\kappa}{\mathrm{d}s} + f_s = 0 \qquad (\text{A } 2a)$$

$$\boldsymbol{e}_n \text{ component}: \quad -EI\frac{\mathrm{d}^2\kappa}{\mathrm{d}s^2} + \kappa T_s + f_n = 0. \qquad (\text{A } 2b)$$

Recall that f_n is related to the pressure drop across the fibre and is given by (3.15). The tangential force, f_s, can be estimated to be $(\mu \partial v_s / \partial n)\, d$, where v_s is the component of velocity locally parallel to the fibre. Hele-Shaw theory does not allow for the no-slip condition to be satisfied at the face of the fibre, so the gradient $\partial v_s / \partial n$ exists to decrease the velocity from a bulk value to zero. Thompson (1968) shows that for simple Hele-Shaw problems there is an inner region the size of the channel depth D where this transition takes place, but for our problem we estimate that it should depend on the depth of the fibre d instead. Thus, we chose d as the size of the inner region, setting the scale for the denominator of the gradient, and taking the average velocity Q/DH as a scale for v_s we estimate that $f_s \sim \mu Q/DH$.

To simplify (A 2), we non-dimensionalize and drop the smallest terms. The pressure and all lengths (including κ^{-1}) are non-dimensionalized according to (3.18). The tangent force f_s is non-dimensionalized by the scale in the previous paragraph. The scale of T_s is set by a balance between the first and second terms of (A 2a), with $T_s \sim EI/H^2$. If instead the scale of T_s had been chosen to balance the first and third terms, with $T_s \sim \mu Q d/D^2$, there would be an inconsistent balance, with the second term being $O((\epsilon D/H)^{-1}) \gg 1$. Keeping the same names for dimensionless quantities, we have

$$\boldsymbol{e_s} \text{ component}: \quad \frac{\mathrm{d}T_s}{\mathrm{d}s} + \kappa \frac{\mathrm{d}\kappa}{\mathrm{d}s} + \frac{D}{6(D+d)} \frac{D}{H} \epsilon f_s = 0 \qquad (A\,3a)$$

$$\boldsymbol{e_n} \text{ component}: \quad -\frac{\mathrm{d}^2 \kappa}{\mathrm{d}s^2} + \kappa T_s - \epsilon[p_+ - p_-] = 0. \qquad (A\,3b)$$

The Hele-Shaw approximation is based on the assumption that $D/H \ll 1$, so we drop the last term in (A 3a). We now integrate this equation in s, and set the integration constant equal to zero since the end of the fibre has no applied tension ($T_s = 0$) and no applied moment ($M = \kappa = 0$). Substituting into (A 3b), we have reduced the system to one ordinary differential equation,

$$\frac{\mathrm{d}^2 \kappa}{\mathrm{d}s^2} + \frac{1}{2}\kappa^3 = -\epsilon[p_+ - p_-]. \qquad (A\,4)$$

This equation is re-dimensionalized to arrive at (3.16).

Appendix B. Non-uniformity of limits and fibre tip divergence

In the asymptotic analysis of §4.3, it was observed that the first-order correction predicts that the horizontal fluid velocity is positive on the left of $x = 0$ but negative on the right. We explained that this is an effect of the distinguished nature of the $x \to 0$ and $\epsilon \to 0$ limits. In this section, we clarify this point and also comment on the divergence of the asymptotic approximations near the fibre tip, which is an important issue for the numerical computations in §5.

It suffices to study a simpler problem: consider flow in the upper half-plane past an infinitesimally thin vertical barrier of height $y = c$ placed at $x = \epsilon$. The exact solution is known through conformal mapping (in fact, this is simply the solution (4.21) shifted in x by an amount ϵ). The complex potential, with $w(z) = p(x, y) + \mathrm{i}\psi(x, y)$ is given by

$$w(z) = \mathscr{A}\sqrt{(z - \epsilon)^2 + c^2}, \qquad (B\,1)$$

with $\mathscr{A} = 1$ for upstream ($x < \epsilon$) and $\mathscr{A} = -1$ for downstream ($x > \epsilon$). Assuming that z is held fixed, we expand (B 1) to obtain an outer expansion for the potential,

$$w_{out}(z) = \mathscr{A}_0 \left(\sqrt{z^2 + c^2} - \epsilon \frac{z}{\sqrt{c^2 + z^2}} + \epsilon^2 \frac{c^2}{2(z^2 + c^2)^{3/2}} + O(\epsilon^3) \right), \qquad (B\,2)$$

with now $\mathscr{A}_0 = \pm 1$ depending on $x \lessgtr 0$.

As mentioned in §4.3, the asymptotic approximation (B 2) predicts a discontinuous velocity at $x = 0$, and this is due to the fact that when we expand (B 1) to obtain (B 2), we fix $z = O(1)$, take $\epsilon \to 0$, and then only afterwards take the limit of $\mathrm{Re}(z) \to 0$ in (B 2) to derive the value along $x = 0$. This is different to taking $x \to 0$ first, and then afterwards expanding for small ϵ.
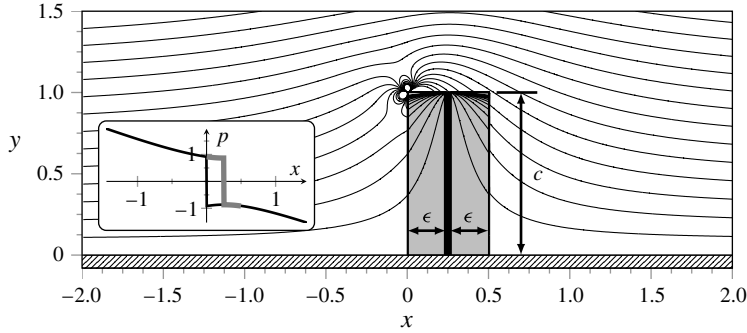
FIGURE 11. Streamlines $\text{Im}(w)$, accurate to $O(\epsilon^2)$, and given in increments of 0.1, for a vertical fibre at $x = \epsilon = 0.25$, with $c = 1$ in an unbounded half-plane. The shaded portion denotes the inner region. The inset shows the pressure $p(x, 0.25)$ with the outer solution (thin) and the inner solution (bold grey).

The key is to introduce a boundary layer of size ϵ near $x = \epsilon$. Near the barrier, we introduce the re-scaled coordinate $X = (x - \epsilon)/\epsilon$, and from (B 1), we obtain

$$w_{in}(X, y) = \mathscr{B}\left(\sqrt{c^2 - y^2} + \epsilon \frac{iXy}{\sqrt{c^2 - y^2}} + \epsilon^2 \frac{c^2 X^2}{2(c^2 - y^2)^{3/2}} + O(\epsilon^3)\right), \quad \text{(B 3)}$$

where $\mathscr{B} = \pm 1$ for $X \lessgtr 0$. Thus, when the value of y is fixed with $0 < y < c$, we use $\text{Re}[w_{out}]$ for the pressure when $x < 0$, $\text{Re}[w_{in}]$ from $0 < x < 2\epsilon$, and again $\text{Re}[w_{out}]$ from $x > 2\epsilon$. Any multiple of ϵ is valid since such boundary layers are only defined within orders of ϵ. An example of such an approximation, accurate to $O(\epsilon^2)$ in each region, is shown in figure 11. There, we see that the introduction of the inner region is necessary to ensure that the streamlines are continuous across the origin.

Note that the introduction of the inner region on the right of the fibre is more for aesthetic reasons, because at higher orders the outer approximation (B 2) for $x > 0$ will begin to 'form' the fibre at $x = \epsilon$. However, for all finite truncations of the series, the velocity at $x = \epsilon$ will continue to be non-zero. The inner region to the right of the fibre provides us with the ability to achieve a zero velocity at $x = \epsilon$ using a finite asymptotic approximation.

Figure 11 also makes it apparent that an additional matching region must be imposed along the path of the tip of the fibre, $z = x + ic$ for $0 < x < \epsilon$, and the worst of this behaviour is seen at the point $z = ic$, where the outer approximation w_{out} in (B 2) is clearly divergent. Of course, these are all of the inherent caveats of using a (singular) asymptotic methodology that depends on shifting the geometry of the problem.

The full problem of §4 is different in that it requires an upper channel wall at $y = 1$, and also the fibre position is no longer fixed at $x = \epsilon$, but is rather at $x = u(y) = \epsilon u_1 + \epsilon^2 u_2 + \cdots$. Consequently, the exact solution is unknown, and we must derive the inner and outer solutions term by term, carefully matching at each order.

However, the qualitative conclusions we have reached for the model problem remain valid for the full problem: the outer asymptotic expansion (4.1a,b) is invalid within a boundary layer of $O(\epsilon)$ near the barrier, and this explains the odd velocities when taking $x \to 0$ in (4.29). The inner solution near the fibre can be determined by rescaling near the fibre and matching outwards to the inner limit of the outer solution.

However, because the fibre is deflected according to (4.25), we assume that this inner problem would need to be determined numerically.

REFERENCES

ABLOWITZ, M. J. & FOKAS, A. S. 2003 *Complex Variables: Introduction and Applications*. Cambridge University Press.

ALBEN, S., SHELLEY, M. & ZHANG, J. 2002 Drag reduction through self-similar bending of a flexible body. *Nature* **420** (6915), 479–481.

ATTIA, R., PREGIBON, D. C., DOYLE, P. S., VIOVY, J. L. & BARTOLO, D. 2009 Soft microflow sensors. *Lab on a Chip* **9** (9), 1213–1218.

AUTRUSSON, N., GUGLIELMINI, L., LECUYER, S., RUSCONI, R. & STONE, H. A. 2011 The shape of an elastic filament in a two-dimensional corner flow. *Phys. Fluids* **23** (6), 063602.

BERTHET, H. 2012 Single and collective fibre dynamics in confined microflows. PhD thesis, ESPCI.

COSENTINO LAGOMARSINO, M., PAGONABARRAGA, I. & LOWE, C. 2005 Hydrodynamic induced deformation and orientation of a microscopic elastic filament. *Phys. Rev. Lett.* **94** (14), 1–4.

DAY, R. F. & STONE, H. A. 2000 Lubrication analysis and boundary integral simulations of a viscous micropump. *J. Fluid Mech.* **416**, 197–216.

DENDUKURI, D., GU, S. S., PREGIBON, D. C., HATTON, T. A. & DOYLE, P. S. 2007 Stop-flow lithography in a microfluidic device. *Lab on a Chip* **7** (7), 818–828.

DENDUKURI, D., PANDA, P., HAGHGOOIE, R., KIM, J. M., HATTON, T. A. & DOYLE, P. S. 2008 Modelling of oxygen-inhibited free radical photopolymerization in a PDMS microfluidic device. *Macromolecules* **41** (22), 8547–8556.

DILUZIO, W. R., TURNER, L., MAYER, M., GARSTECKI, P., WEIBEL, D. B., BERG, H. C. & WHITESIDES, G. M. 2005 Escherichia coli swim on the right-hand side. *Nature* **435** (7046), 1274.

GERVAIS, T., EL-ALI, J., GÜNTHER, A. & JENSEN, K. F. 2006 Flow-induced deformation of shallow microfluidic channels. *Lab on a Chip* **6** (4), 500–507.

GUGLIELMINI, L., KUSHWAHA, A., SHAQFEH, E. S. G. & STONE, H. A. 2012 Buckling transitions of an elastic filament in a viscous stagnation point flow. *Phys. Fluids* **24** (12), 123601.

JOUNG, C. G., PHAN-THIEN, N. & FAN, X. J. 2001 Direct simulation of flexible fibres. *J. Non-Newtonian Fluid Mech.* **99**, 1–36.

LAUGA, E. & POWERS, T. R. 2009 The hydrodynamics of swimming microorganisms. *Rep. Prog. Phys.* **72** (9), 096601.

MILNE-THOMSON, L. M. 1968 *Theoretical Hydrodynamics*. Dover Publications.

PAÏDOUSSIS, M. P. 2004 *Fluid–Structure Interactions, vol. 1–2*. Academic Press.

POZRIKIDIS, C. 1992 *Boundary Integral and Singularity Methods for Linearized Viscous Flow*. Cambridge University Press.

POZRIKIDIS, C. 2011 Shear flow past slender elastic rods attached to a plane. *International Journal of Solids and Structures* **48** (1), 137–143.

QIAN, B., POWERS, T. & BREUER, K. 2008 Shape transition and propulsive force of an elastic rod rotating in a viscous fluid. *Phys. Rev. Lett.* **100** (7), 078101.

RUSCONI, R., LECUYER, S., GUGLIELMINI, L. & STONE, H. A. 2010 Laminar flow around corners triggers the formation of biofilm streamers. *J. Roy. Soc. Int.* **7** (50), 1293–1299.

SEMIN, B., HULIN, J. P. & AURADOU, H. 2009 Influence of flow confinement on the drag force on a static cylinder. *Phys. Fluids* **21** (10), 103604.

SNEDDON, I. N. 1966 *Mixed Boundary Value Problems in Potential Theory*. Wiley.

SQUIRES, T. & QUAKE, S. 2005 Microfluidics: Fluid physics at the nanoliter scale. *Rev. Mod. Phys.* **77** (3), 977–1026.

STOCKIE, J. M. & GREEN, S. I. 1998 Simulating the motion of flexible pulp fibres using the immersed boundary method. *J. Comp. Phys.* **147** (1), 147–165.

STONE, H. A., STROOCK, A. D. & AJDARI, A. 2004 Engineering flows in small devices. *Ann. Rev. Fluid Mech.* **36** (1), 381–411.

THOMPSON, B. W. 1968 Secondary flow in a Hele–Shaw cell. *J. Fluid Mech.* **31** (2), 379–395.

TUCK, E. O. 1964 A systematic asymptotic expansion procedure for slender ships. *J. Ship Res.* **8** (1), 639–668.

VANDEN-BROECK, J.-M. 2010 *Gravity-Capillary Free-Surface Flows*. Cambridge University Press.

WANDERSMAN, E., QUENNOUZ, N., FERMIGIER, M., LINDNER, A. & DU ROURE, O. 2010 Buckled in translation. *Soft Matt.* **6** (22), 5715.

WIGGINS, C. & GOLDSTEIN, R. 1998 Flexive and propulsive dynamics of elastica at low Reynolds number. *Phys. Rev. Lett.* **80** (17), 3879–3882.

YOUNG, Y.-N., DOWNS, M. & JACOBS, C. R. 2012 Dynamics of the primary cilium in shear flow. *Biophys. J.* **103** (4), 629–639.

YU, T. S., LAUGA, E. & HOSOI, A. E. 2006 Experimental investigations of elastic tail propulsion at low Reynolds number. *Phys. Fluids* **18** (9), 091701.

‡ The original version of this article was published with A. Lindner's name incorrectly spelled. A notice detailing this has been published and the error rectified in the online PDF and HTML copies.